

## Research Article

# A W-Band Radiometer with the Offset Parabolic Antenna for Radiometric Measurements

**Li Wu, Shu-sheng Peng, Jian-zhong Xu, and Ze-long Xiao**

*School of Electronic and Optical Engineering, Nanjing University of Science & Technology, Xiaolingwei Avenue 200, Xuanwu District, Nanjing, Jiangsu 210094, China*

Correspondence should be addressed to Li Wu; [li\\_wu@njust.edu.cn](mailto:li_wu@njust.edu.cn)

Received 18 September 2015; Revised 5 December 2015; Accepted 3 January 2016

Academic Editor: Atsushi Mase

Copyright © 2016 Li Wu et al. This is an open access article distributed under the Creative Commons Attribution License, which permits unrestricted use, distribution, and reproduction in any medium, provided the original work is properly cited.

This paper deals with the development of a W-band noise-adding radiometer which combines the millimeter-wave (MMW) radiometric measurements with a high-resolution imager. The offset parabolic antenna is presented to achieve an accurate measurement and a high resolution. To reduce the cross-polarization level of the antenna, a multimode feed horn with a multistep structure is proposed to match the focal region fields of the reflector. It has advantages over the corrugated horns in lower mass and easier manufacturing. In addition, due to an unavoidable settling time for the noise-adding radiometer output signal passing through the low-pass filter, a theoretical criterion for the optimum duty cycle determination to reject extraneous contributions from the transient is proposed in this paper. The appropriate duty cycle threshold is 0.33 for the developed W-band radiometer. Also, a geometric correction method is presented to correct the obtained passive image suffering from a distortion for a better image interpretation. Preliminary experimental results are given to illustrate and verify the presented techniques.

## 1. Introduction

Due to the advantages of passive and covert operations and smog penetration, the MMW radiometer systems are often used for short to mid-range observations and detections in surveillance, reconnaissance, and target tracking on seekers or unmanned aerial vehicle platforms [1, 2]. A similar application is the improved surveillance and protection of sensitive infrastructures of nuclear power plants or mass events [3, 4]. It is also employed for remote sensing of volcanic terrain at active lava domes in almost all weather conditions from ground-based survey points [5]. In the above applications, MMW sensors interact with scenario where they operate and take autonomous decisions, which are made based on their perception of the surroundings. It is essential to measure the radiation of the objects and the operation environment accurately to evaluate the performances of the MMW sensors. As the ceramic weapons and the plastic explosive cannot be detected by conventional metal detection techniques, MMW radiometric imaging is increasingly being seen for personnel screening applications [6, 7]. And an accurate radiometric measurement of interested items is also necessary to evaluate

the performances of MMW imaging systems and to offer database for the contraband items detection, classification, and identification [8, 9].

To achieve an accurate measurement and a higher spatial resolution, a high-gain low sidelobe level antenna is essential for the radiometer system [10]. The offset parabolic antennas bring attractive properties over the axially symmetric ones in lower sidelobes and higher main beam efficiencies and are considered to be more suitable for radiometry applications [11, 12]. However, the asymmetric field distribution in the reflector leads to a higher cross-polarization level. To reduce the cross-polarization of offset reflector antennas, corrugated horns are often used as primary feeds to match the focal region fields of the reflector antenna [13], whereas it brings the expense of aperture efficiency, manufacturing complexity, and mass [14]. In this paper, a compact multimode feed horn is proposed with a small aperture diameter to achieve the cross-polarization reduction. Also the presented feed can be more easily manufactured.

Various types of radiometers such as Dicke switching [15], noise injection [10], and noise-adding [16] have been applied for radiometric measurements. And the noise-adding

radiometer is employed in the developed system since it is advantageous over other radiometers for minimal RF hardware added [16]. Due to an unavoidable settling time for the signal passing through the low-pass filter, the digitalized radiometer output samples near the noise source switching boundaries must be excluded by setting a duty cycle. Though the threshold of duty cycle was set as 0.3 in [16], its determination process was not presented in that paper. And the duty cycle for the noise-adding radiometer with different parameters should be different. However, there is not any published references for the optimum duty cycle determination to our knowledge. To deal with this issue, a theoretical criterion for duty cycle determination is provided in this paper. In addition, as the passive image obtained by mechanical two-dimensional scanning suffers from a barrel distortion, a distorted image correction method is presented in this paper to achieve a better interpretation.

The rest of this paper will be organized as follows. Section 2 demonstrates the radiometer system architecture and describes the design of radiometer receiver in detail. Also the W-band offset parabolic antenna with a multistep structure multimode feed is proposed in this section. The radiometer measurement model is established and the duty cycle for a rejection of extraneous contributions from the low-pass filter is determined in theory in Section 3. Preliminary experiment results are presented in Section 4 to verify the radiometer system. The last section is the conclusion.

## 2. The W-Band Radiometer System

*2.1. Introduction of the System.* Figure 1 illustrates the block diagram of the developed W-band radiometer system which is composed of the offset parabolic antenna, the radiometer front end, the intermediate frequency (IF) section, the video signal processing module, the central processing and control embedded system, the Global Positioning System and BeiDou Navigation Satellite System (GPS/BDS) integrated multimode receiver, the two-dimensional scanner, the servo controller, the data acquisition board, and the industrial personal computer (IPC). The front end and the IF component are all housed in an insulated box whose temperature stays stable within 40–45°C in outdoor operations with a variability of 0.2 K accomplished by a PID thermal controller. The employed thermal control measures are helpful to stabilize the receiver because the gain of the front end and IF component is sensitive to the temperature variation. The whole radiometer receiver is contained in the radiometer box which can be placed on the two-dimensional scanner. As the radiometer system has a loose requirement for imaging time in the applications of this paper, a low-cost mechanical scanning manner is applied in spite of a lower imaging speed. The servo controller, the data acquisition board, and the IPC are mounted in a control cabinet for the conveniences of operation. An overview of the developed radiometer system is presented in Figure 2.

While working, the W-band radiometer placed on the scanner is driven by the servo controller which has an angular measurement error of less than 0.05°. It can observe a scene

at a given angle or within a certain angular range. The information of the radiometer system like output voltage, current pointed position, and measurement results is all displayed in both of the embedded central processing and control unit and IPC. Moreover, the GPS/BD receiver provides an information of time, latitude, and longitude of operation.

*2.2. Receiver Description.* The radiometer receiver consists of the single-pole double-throw (SPDT) PIN switch, the directional coupler, the isolator, the local oscillator (LO), the mixer, the IF amplifier, the square-law detector, and the video signal processing circuit. The block diagram of the receiver is shown in Figure 3.

The LO is a critical element in the receiver development. Due to a finite mixer LO-RF isolation, the LO signal leakage from LO port to RF port of the mixer will result in reverse radiation and deteriorate the radiometer's performance greatly [17]. The employed LO with a Gunn diode shows a frequency of 94.5 GHz, with output power of 14 dBm and typical frequency stability of 5 MHz/°C. Besides, an isolator is placed between the coupler and the mixer to reduce the effects of reverse radiation, which performs a maximum insertion loss of 0.9 dB and a minimum isolation of 18 dB at operating frequencies. The exploited balanced double-sideband (DSB) mixer characterizes a maximum conversation loss of 9 dB, a noise figure of 8 dB, and a typical LO-RF isolation of 18 dB. Also a preamplifier with a bandwidth of 100–2500 MHz and a gain of 20 dB is integrated within the mixer to improve the overall receiver performance.

Additionally, the noise injected by the noise source via a directional coupler is taken as the reference hot load to improve the measurement accuracy. The solid noise source employed is featured by an ENR of 14 dB at the receiver operation frequencies; that is, the increased noise temperature is around 7284 K when the noise source is switched on. To prevent a saturation of the receiver caused by such a large noise power, a directional coupler with a coupling factor of -13 dB and an insertion loss of 1 dB is used. The downconverted signal of the mixer is amplified by an IF amplifier and is then connected to a square-law detector whose output voltage is proportional to the noise power. The input to the square-law detector must be within its linear range and must be low enough not to saturate the device. The realized IF amplifier component, which is characterized by the centre frequency of 1.5 GHz, a bandwidth of 2 GHz, a noise figure of 1.5 dB, and a maximum gain of 36 dB, consists of a band-pass filter and a two-stage monolithic amplifier and a voltage controlled attenuator to adjust the system gain. The video signal amplification is realized with the instrumentation amplifiers, and the analogue integrator is composed by a simple passive resistor-capacitor (RC) filter with a cutoff frequency of approximately 20 kHz. The video amplifier output is then connected to the central processing and control unit to extract brightness temperature estimations of the observed scene.

*2.3. Design of the W-Band Offset Parabolic Antenna.* In order to achieve a better measurement accuracy and space resolution, a high-gain low sidelobe level and low Voltage Standing

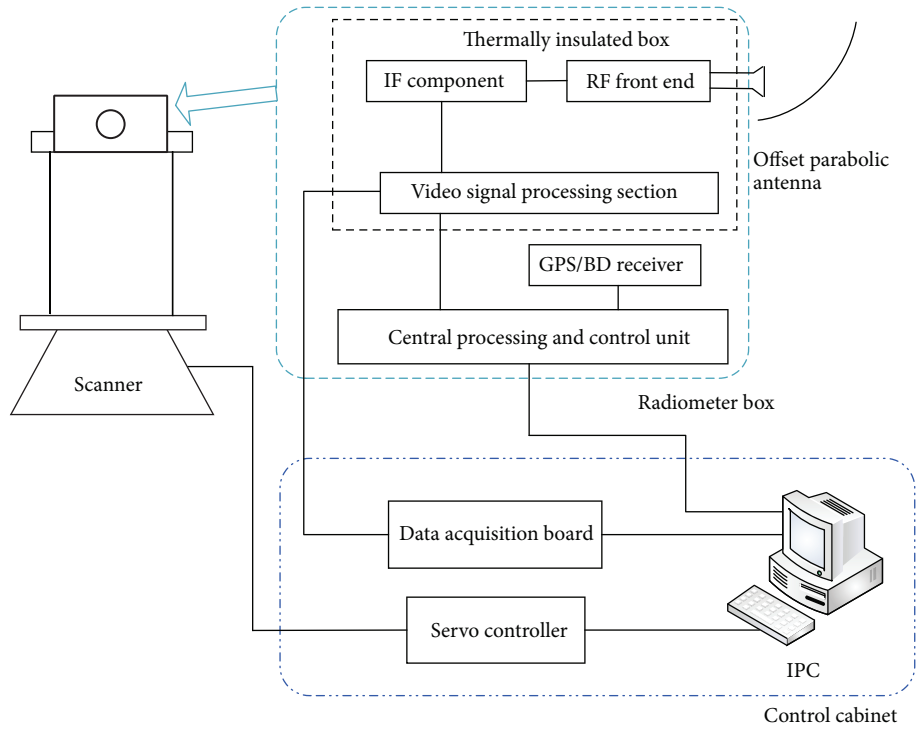


FIGURE 1: Block diagram of the W-band radiometric imaging system.



FIGURE 2: A picture of the W-band radiometer system.

Wave Ratio (VSWR) antenna is of great significance for the radiometric systems. Hence, a large aperture W-band offset reflector antenna is presented to meet the above requirements in the paper. However, the offset reflector antenna will suffer from a high cross-polarization level due to the structure asymmetry [18]. In order to reduce the cross-polarization level, a multimode feed horn is proposed.

The geometry of the offset parabolic antenna, which is composed of the offset reflector and the feed, is shown in Figure 4. The offset reflector is shaped by the intersection of a cylindrical surface and a paraboloid defined by  $z =$

$(x^2 + y^2)/4f$ . That is to say, the offset reflector has a circular projected aperture with the diameter of  $D$ .

In Figure 4,  $f$  denotes the focal length of the paraboloid and it is 125 mm for the designed antenna and  $\psi_0$  indicates the offset angle. Due to an asymmetric structure, the cross-polarization level of an offset parabolic antenna is impacted seriously by the offset angle whose value is set as  $\psi_0 = 5.7^\circ$  based on the simulation. And this shapes an elliptic reflector with a longer dimension of 300 mm and with a projected aperture diameter of  $D = 250$  mm. Moreover, the offset height  $d$  is set to be 12.5 mm to ensure that the feed would not block the ray from the bottom reflector surface.

To achieve a lower sidelobe level and cross-polarization level, the conjugate match technique is employed which ensures that the feed field distribution is the conjugate match of the focal plane field of offset reflector. The induced currents on the reflector mirror surface can be obtained with the surface current method and then the focal plane field distribution is derived by employing the Stratton-Chu formulas. Also for the feed of offset parabolic reflector, it requires a lower cross-polarization and no side-lobes subtended by the reflector [19]. Hence, a multimode feed horn with a multistep structure is proposed to meet the above requirements. The overview of geometry of the multimode feed horn is illustrated in Figure 5.

As can be seen from the figure, the whole multimode feed horn consists of seven parts. The section from "AB" to "CD" is the conversion stage from a standard waveguide to a square waveguide, where  $TE_{10}$  and  $TE_{01}$  mode are propagating at the output. The parts from "DE" to "EF" are the conversion section from a square waveguide to a circular waveguide with

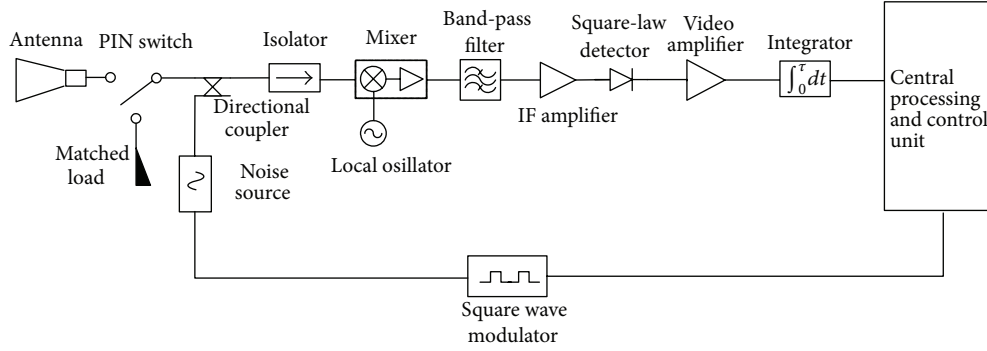


FIGURE 3: Illustration of the receiver block diagram.

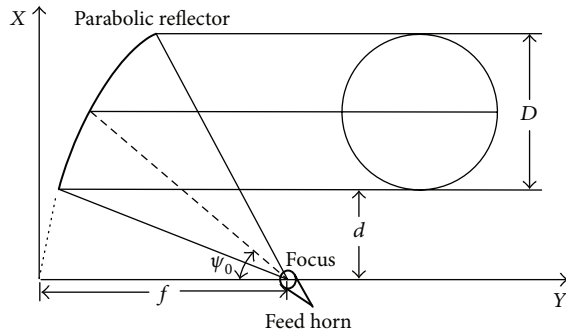


FIGURE 4: Geometry of the offset parabolic antenna designed for radiometric imaging.

the only  $TE_{11}$  mode propagation at the output, and the last parts are an excitation section where  $TE_{11}$ ,  $TM_{11}$ , and  $TE_{12}$  mode are propagating simultaneously, while other unwanted high-order modes are suppressed. The lists of all geometry parameters are presented in Table 1.

As shown in Figure 6, the fabricated offset parabolic antenna is simulated with FEKO and measured in the anechoic chamber. The simulation and measurement results of primary polarization and cross-polarization of the antenna at frequency 94.5 GHz are shown in Figures 7(a) and 7(b), respectively.

As seen from Figure 7 that the measurements show a good general agreement with the simulations. The detailed measurement results at frequency of 91 GHz, 94.5 GHz, and 97 GHz are presented in Table 2.

From the results in Table 2, we can know that the gain is larger than 41.2 dB, sidelobe level is less than  $-25.5$  dB, half-power beamwidth is less than  $1^\circ$ , and cross-polarization level is below  $-31.4$  dB at frequencies 91–97 GHz.

### 3. System Measurement Model

While the radiometer is working, the input noise from the antenna or the reference matched load is added with the injected noise generated by the noise source, which is modulated with a periodic square wave. When the noise source is switched on and off, the video amplifier's output

which is proportional to the input noise power can be expressed by the following equations, respectively:

$$\begin{aligned} V_{ON} &= C_d G k B (T_a + T_R + T_{on}) + V_z, \\ V_{OFF} &= C_d G k B (T_a + T_R + T_{off}) + V_z, \end{aligned} \quad (1)$$

where  $C_d$  is the square-law detector sensitivity,  $G$  is the receiver gain,  $k$  is the Boltzmann constant,  $B$  is the system bandwidth predetection,  $T_a$  is the antenna temperature,  $T_R$  is the equivalent input noise temperature of the radiometer receiver,  $T_{on}$  and  $T_{off}$  are the injected noise temperature when the noise source is on and off, respectively, and  $V_z$  is the zero offset voltage of the video amplifier.

A variable  $K_x$  is defined as

$$\begin{aligned} K_x &= \frac{V_{OFF}}{(V_{ON} - V_{OFF})} \\ &= \frac{(T_a + T_R + T_{off})}{\Delta T_N} + \frac{V_z}{(V_{ON} - V_{OFF})}, \end{aligned} \quad (2)$$

where  $\Delta T_N = T_{on} - T_{off}$  is the difference of the injected noise temperature between the noise source's on and off status, and it can be expressed by

$$\Delta T_N = T_{on} - T_{off} = C T_o ENR, \quad (3)$$

where  $C$  is the coupling factor of the directional coupler,  $T_o = 290$  K is the IEEE standard temperature, and  $ENR$  is the excess noise ratio of the noise source. To eliminate impacts of the receiver equivalent noise temperature and the zero offset voltage of the video amplifier, the periodic calibration technique in [20] is exploited; that is, the scene and the reference load are observed alternatively by controlling the SPDT PIN switch. So the observed brightness temperature of  $T_a$  can be resolved by

$$T_a = T_m - \Delta T_N (K_m - K_x), \quad (4)$$

where  $T_m$  is the physical temperature of the matched load and  $K_m$  is the defined voltage ratio in (2) for the observation of matched load. The radiometer output signal is commonly digitized with the data acquisition board and processed to obtain the voltage ratio. As illustrated in Figure 8, a typical

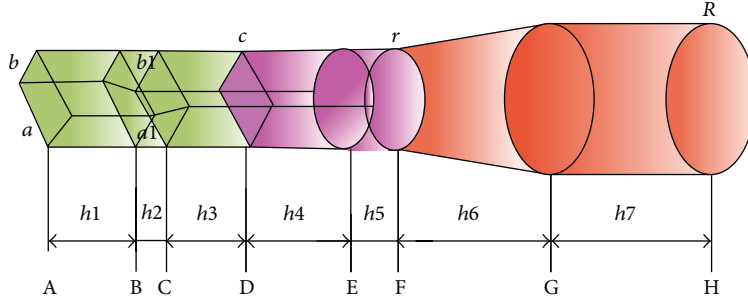


FIGURE 5: Geometry of multimode horn feed.

TABLE 1: Geometry parameters lists of the multimode feed horn.

$h1$ (mm)	$h2$ (mm)	$h3$ (mm)	$h4$ (mm)	$h5$ (mm)	$h6$ (mm)	$h7$ (mm)
3	1.2	3	3.7	1.85	5.56	5.56
$a$ (mm)	$b$ (mm)	$a1$ (mm)	$b1$ (mm)	$c$ (mm)	$r$ (mm)	$R$ (mm)
1.27	2.54	1.64	2.23	1.91	1.15	2.22

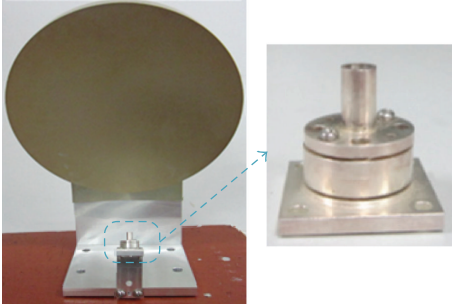


FIGURE 6: A picture of the designed W-band offset parabolic antenna.

radiometer output is a square wave and it is obvious that there is a transient response of the antialiasing and low-pass filters near the switching boundaries.

Similar to the gated integration processing method given in [16], a series of output samples are averaged over the individual time gates to form the integrated on and off voltages

$$\overline{V_{\text{ON}}} = \frac{1}{LdT} \sum_{i=0}^{L-1} \int_{(0.5-d)T}^{0.5T} v(t+iT) dt, \quad (5)$$

$$\overline{V_{\text{OFF}}} = \frac{1}{LdT} \sum_{i=0}^{L-1} \int_{(1-d)T}^T v(t+iT) dt,$$

where  $T$  is the switching period of the noise source,  $d$  is a duty cycle of the time gate relative to the switching period, and  $L$  is the switching periods per an integration time. Though the duty cycle was set at or below 0.3 to reject extraneous contributions from the transient response of the filter in [16], the determination of this threshold is not described in the literature. As a simple RC low-pass filter is employed as the

integrator in the receiver, its time response to the Heaviside function with a step  $V_T$  can be written as

$$V_{\text{RC}}(t) = \begin{cases} 0 & t < 0 \\ V_T \exp\left(-\frac{t}{\tau_{\text{RC}}}\right) & t \geq 0, \end{cases} \quad (6)$$

where  $\tau_{\text{RC}}$  is the time constant of the RC low-pass filter. It can be seen from this formula that a settling time is required to obtain a correct integrator output value. Supposing that  $N$  is the number of the analog-to-digital converter (ADC) bits and LSB is the least significant bit, the voltage step  $V_T$  can be expressed with the full-scale voltage of ADC by

$$V_T = \rho 2^N \text{LSB}, \quad (7)$$

where  $\rho$  is the ratio of the voltage step  $V_T$  to the full-scale voltage of ADC. It takes a settling time of  $t_{\text{set}}$  for a step signal with the amplitude of  $V_T$  passing through the integrator to reach a resolution of the ADC; that is,

$$V_T \left(1 - \exp\left(-\frac{t_{\text{set}}}{\tau_{\text{RC}}}\right)\right) = V_T - \frac{\text{LSB}}{2}. \quad (8)$$

So the settling time of the integrator can be obtained from (8) by the following expression:

$$t_{\text{set}} = \tau_{\text{RC}} [(N+1) \ln 2 + \ln \rho] = \tau_{\text{RC}} \eta_{\text{set}}, \quad (9)$$

where  $N$  is the number of the ADC bits and  $\eta_{\text{set}}$  is defined as the settling time coefficient which is a ratio of the settling time to the integrator time constant. To illustrate how the settling time coefficient changes with the number of ADC bits and the voltage step value in detail, a plot of the settling time coefficients under different values of  $N$  and  $\rho$  is presented in Figure 9.

It can be seen from Figure 9 that a higher  $N$  results in a larger settling time coefficient under the same voltage step value; that is to say, a higher resolution ADC will

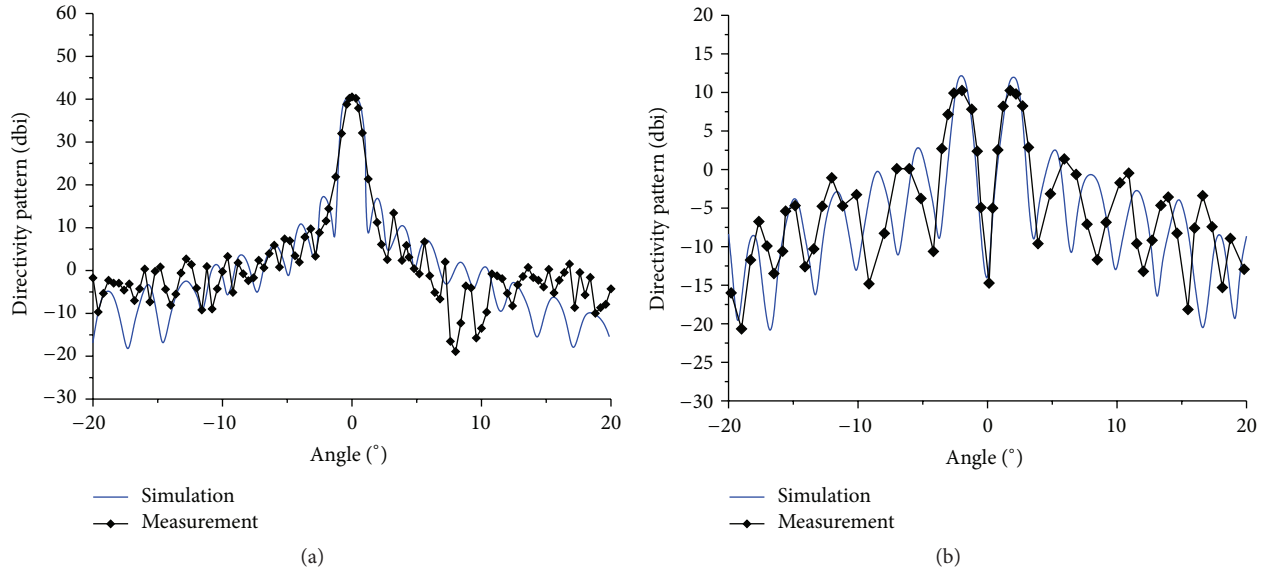


FIGURE 7: The simulation and measurement results of (a) primary polarization and (b) cross-polarization at frequency 94.5 GHz.

TABLE 2: Measurement results of the W-band parabolic offset antenna.

Frequency (GHz)	Gain (dB)	Sidelobe level (dB)	Half-power beamwidth ( $^{\circ}$ )	Cross-polarization level (dB)
91	41.26	-25.68	0.98	-31.6
94.5	41.41	-25.87	0.96	-31.47
97	41.98	-25.56	0.92	-31.8

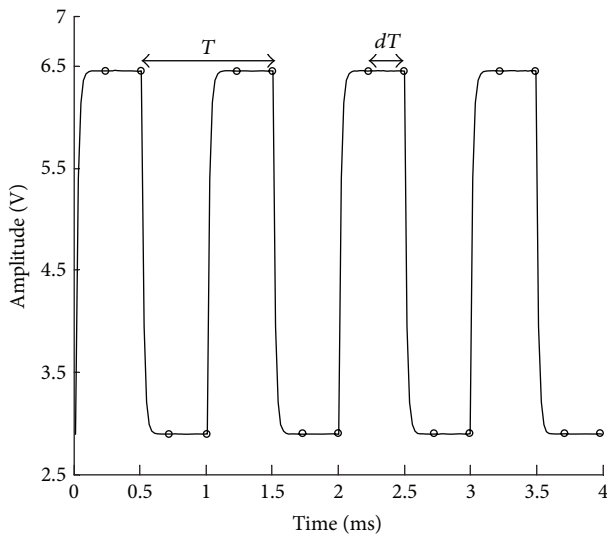


FIGURE 8: A typical output of the designed radiometer.

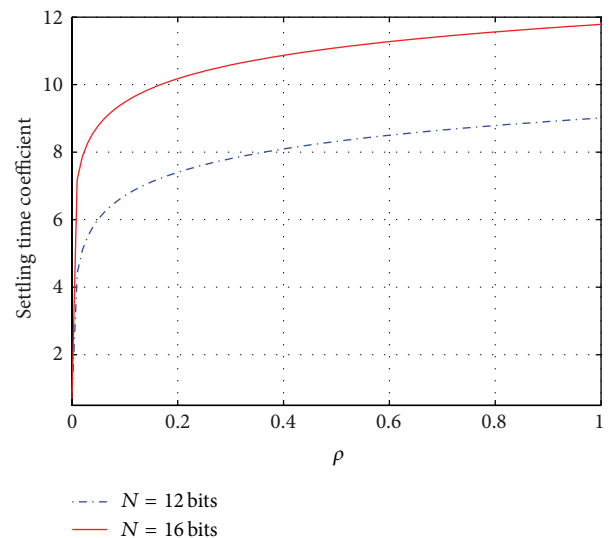


FIGURE 9: Plot of the settling time coefficients under different values of  $N$  and  $\rho$ .

require a longer settling time. Also, the settling time coefficient increases with the natural logarithm of the voltage step value, and a larger voltage step will contribute a larger settling time. For the common 12-bit and 16-bit ADCs, the settling time is

about 9 and 11.8 times of the time constant, respectively, with a voltage step of the ADC full-scale voltage.

In the developed W-band radiometer, a 16-bit ADC is employed and the effective integration time is  $16 \mu\text{s}$  for the

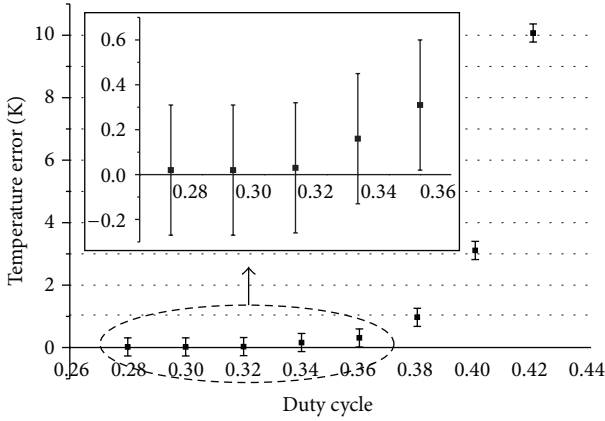


FIGURE 10: Plot of the temperature error with duty cycles ranging from 0.28 to 0.42 by a step of 0.02.



FIGURE 11: A picture of the imaging scenario.

integrator with a cutoff frequency of 20 kHz. In addition, a step of 30% of full-scale voltage is caused by the injected noise on top of the receiver noise, and the obtained settling time is approximately 0.17 ms by inserting the above parameters into (9). Thereafter, the duty cycle should be less than 0.33 considering that the switching frequency of the noise source is 1 kHz.

#### 4. Preliminary Experiment Results

Initially, the developed radiometer was calibrated with the tipping curve calibration method [21, 22] which takes the atmosphere under clear weather condition as a reference load because of the inconvenient operation in conventional liquid nitrogen calibration. Several groups of measurement data at the zenith angles of 0°, 48°, 60°, 66.5°, and 70.5° were processed to determine the system calibration coefficients by applying atmospheric radiation transfer theory.

Subsequently, several experiments were conducted to evaluate the correctness of theoretical guideline for the duty cycle determination. An ambient absorber was observed continuously with the calibrated radiometer for about 30 minutes. And several groups of data samples chosen from the digitalized video amplifier output signal with different duty cycles were processed to retrieve the brightness temperature of the absorber. The number of time gates was adjusted to achieve an integration time of 1 s over which the output samples were averaged to form an integrated on and off

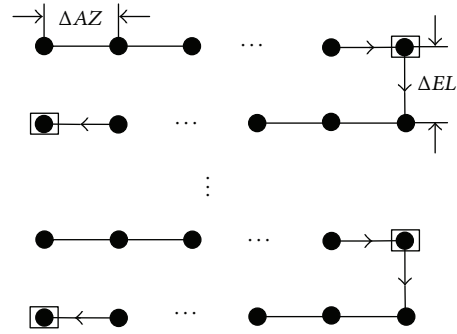


FIGURE 12: Sketch of scanning path for the scenario imaging.

voltage. Also, the physical temperature of the absorber was monitored continuously with a precise thermometer. The temperature errors between the observed brightness temperature and monitored physical temperature were taken as a tool to evaluate the impacts on system measurement accuracy of duty cycles. A plot of the temperature error varying with the duty cycle whose range is from 0.28 to 0.42 by a step of 0.02 is presented in Figure 10.

From the figure we can find that the logarithm of temperature error increases approximately linearly with the duty cycle in the range from 0.32 to 0.42. It is because the output voltage error, which is proportional to the observed brightness temperature error of the radiometer, relates to the duty cycle in an exponential form as shown in (8). And the temperature error is negligible when the duty cycle is smaller than 0.34. It validates the theoretical economic duty cycle threshold of 0.33 which is derived from the expression of settling time for the developed W-band radiometer in Section 3. Also it can be seen that the measurement variances under different duty cycles are almost the same due to the same radiometric resolution.

In addition, outdoor imaging experiments were conducted on the roof of a building in Nanjing. The day was clear with the surface temperature around 300 K. A picture of the imaging scenario is shown in Figure 11 and the distance between the radiometer and the wall is about 20 m. The azimuth angle starts from  $-30^\circ$  to  $30^\circ$  and the elevation angle range is  $0-20^\circ$ . Considering the angular resolution of  $1^\circ$  and the Nyquist sampling criterion, the scan step is set as  $0.5^\circ$ . The sketch of scanning path is presented in Figure 12, and the whole distance lasts approximately 20 minutes. The radiometer output signal is acquired and processed after each step during a continuous antenna movement to obtain a pixel. To achieve a compromise between scanning speed and measurement accuracy, the reference matched load is only observed at the ending point of each scanning line (depicted by a square in Figure 12), and observation results are derived from the measurement data of the field of view. The obtained imaging result is presented in Figure 13.

It is evident that the obtained passive image suffered from a barrel distortion due to the fact that the two-dimensional scanner moves in spherical coordinates. Therefore, it necessitates a geometric correction for image processing. To correct the distorted image, the mathematical geometric correction

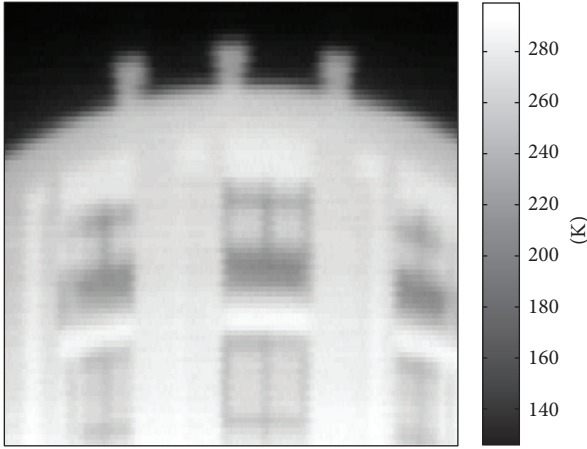


FIGURE 13: A passive image of the building suffered from distortion.

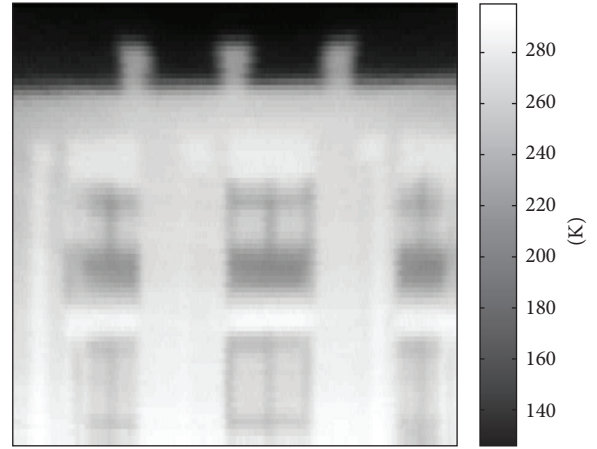


FIGURE 15: The corrected passive image of the building.

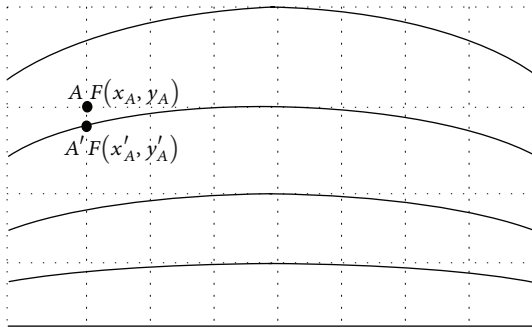


FIGURE 14: Illustration of correction for the distorted image.

model whose parameters are determined by the scanning conditions is initially set up. The image correction process can be divided into two steps: (1) establish mapping coordinate relationship between the distortion pixel and reference pixel and determine the real pixel coordinate; (2) determine the gray value of each pixel using the interpolation.

As shown in Figure 14,  $A'$  is a pixel in the distorted image of  $F(x', y')$  with the coordinate of  $(x'_A, y'_A)$ ,  $A$  is the mapping pixel of  $A'$  in the reference image of  $F(x, y)$  with the coordinate of  $(x_A, y_A)$ . The mapping relationships between  $A$  and  $A'$  can be described as in the following equations:

$$\begin{aligned} x_A &= x'_A, \\ y_A &= \sec \theta_{AZ} \cdot y'_A, \end{aligned} \quad (10)$$

where  $\theta_{AZ}$  denotes the azimuth angle. When corrected, the pixel of  $A'$  in the distorted image of  $F(x', y')$  is simply assigned to the mapping pixel of  $A$ . However, it is necessary to note that the interpolation technique is exploited to fill some pixels due to nonlinear mapping relationship. The corrected passive image of the scenario is shown in Figure 15.

Compared with the distorted image, the corrected one is intuitive and convenient for the analysis. From the figure it is shown that brightness temperature of the scenario varies from 140 K to 280 K, where the coldest sky appears dark, whereas the wall has the highest temperature. The profile of

the building is clear due to a large contrast between it and the cold sky. The details of the windows can be also observed for the reflectivity differences between the glasses and metallic bars and it shows the high angular resolution of the designed offset parabolic antenna.

## 5. Conclusion

In this paper, we have demonstrated a W-band noise-adding radiometer system with the large aperture offset parabolic antenna for radiometric measurements. An offset parabolic antenna with a projected aperture diameter of 250 mm is presented. And a multistep structure multimode feed horn is proposed to guarantee the performances of the offset parabolic antenna. The antenna measurement results show that the half-power beamwidth is less than  $1^\circ$ , the sidelobe level is below  $-25.5$  dB, and the cross-polarization level is below  $-31.4$  dB at operating frequencies.

To reject extraneous contributions from the transient responses of the integrator, the selection of duty cycle value is derived in theory. It is proved that a higher resolution ADC and a larger voltage step caused by the injected noise will contribute a lower duty cycle. For the developed radiometer which employs a switching frequency of 1 kHz, a 16-bit ADC, an integrator with cutoff frequency of 20 kHz, and the duty cycle should be less than 0.33. Also a periodic calibration technique is employed to remove drifts of the receiver equivalent noise temperature and the zero offset voltage of the video amplifier. And a correction model is proposed to correct the passive image which suffers from a distortion due to spherical scanning.

The designed W-band radiometer in this paper stays focused on the measurement accuracy besides imaging function and is suitable for the applications which have requirements for the measurement accuracy such as measurement of MMW radiation properties of matter and evaluation of smart MMW sensors operation environment. The improvement of scanning manner to reduce imaging time will be the work of further research.

## Conflict of Interests

The authors declare that there is no conflict of interests regarding the publication of this paper.

## Acknowledgments

This work was supported by the National Natural Science Foundation of China (nos. 61301213 and 61501234) and the Natural Science Foundation of Jiangsu Province (no. SBK20130768).

## References

- [1] M. Peichl, S. Dill, M. Jirousek, and H. Süß, "Microwave radiometry—imaging technologies and applications," in *Proceedings of the Wave Propagation in Communication, Microwave Systems and Navigation (WFMN '07)*, pp. 75–83, Chemnitz, Germany, July 2007.
- [2] F. Soldovieri, A. Natale, V. Gorishnyak, A. Pavluhenko, A. Denisov, and L. Chen, "Radiometric imaging for monitoring and surveillance issues," *International Journal of Antennas and Propagation*, vol. 2013, Article ID 272561, 8 pages, 2013.
- [3] N. Gopalsami, S. Bakhtiari, T. W. Elmer II, and A. C. Raptis, "Application of millimeter-wave radiometry for remote chemical detection," *IEEE Transactions on Microwave Theory and Techniques*, vol. 56, no. 3, pp. 700–709, 2008.
- [4] N. Gopalsami, H. T. Chien, A. Heifetz, E. R. Koehl, and A. C. Raptis, "Millimeter wave detection of nuclear radiation: an alternative detection mechanism," *Review of Scientific Instruments*, vol. 80, no. 8, Article ID 084702, 2009.
- [5] D. G. MacFarlane, H. M. Odbert, D. A. Robertson, M. R. James, H. Pinkerton, and G. Wadge, "Topographic and thermal mapping of volcanic terrain using the AVTIS ground-based 94-GHz dual-mode radar/radiometric imager," *IEEE Transactions on Geoscience and Remote Sensing*, vol. 51, no. 1, pp. 455–472, 2013.
- [6] Z. L. Xiao, T. Y. Hu, J. Z. Xu, and L. Wu, "Millimetre-wave radiometric imaging for concealed contraband detection on personnel," *IET Image Processing*, vol. 5, no. 5, pp. 375–381, 2011.
- [7] A. Luukanen, R. Appleby, M. Kemp, and N. Salmon, "Millimeter-wave and terahertz imaging in security applications," in *Terahertz Spectroscopy and Imaging*, pp. 491–520, Springer, Berlin, Germany, 2013.
- [8] L. C. Li, J. Y. Yang, G. L. Cui, Z. Jiang, and X. Zheng, "Method of passive MMW image detection and identification for close target," *Journal of Infrared, Millimeter, and Terahertz Waves*, vol. 32, no. 1, pp. 102–115, 2011.
- [9] S. Yeom, D.-S. Lee, Y. S. Jang, M.-K. Lee, and S.-W. Jung, "Real-time concealed-object detection and recognition with passive millimeter wave imaging," *Optics Express*, vol. 20, no. 9, pp. 9371–9381, 2012.
- [10] F. T. Ulaby, R. K. Moore, and A. K. Fung, *Microwave Remote Sensing: Active and Passive. Volume 1-Microwave Remote Sensing Fundamentals and Radiometry*, Artech House, Norwood, Mass, USA, 1981.
- [11] Z. A. Pour and L. Shafai, "A simplified feed model for investigating the cross polarization reduction in circular-and elliptical-rim offset reflector antennas," *IEEE Transactions on Antennas and Propagation*, vol. 60, no. 3, pp. 1261–1268, 2012.
- [12] A. Durić, A. Magun, A. Murk, C. Mätzlermatzler, and N. Kämpferkampfer, "The fully polarimetric imaging radiometer SPIRA at 91 GHz," *IEEE Transactions on Geoscience and Remote Sensing*, vol. 46, no. 8, pp. 2323–2336, 2008.
- [13] S. B. Sharma, D. Pujara, S. B. Chakrabarty, and R. Dey, "Cross-polarization cancellation in an offset parabolic reflector antenna using a corrugated matched feed," *IEEE Antennas and Wireless Propagation Letters*, vol. 8, pp. 861–864, 2009.
- [14] S. Rao, L. Shafai, and S. K. Sharma, *Handbook of Reflector Antennas and Feed Systems Volume III: Applications of Reflectors*, Artech House, Norwood, Mass, USA, 2013.
- [15] T. Sugiura, H. Hirata, J. W. Hand et al., "Five-band microwave radiometer system for noninvasive brain temperature measurement in newborn babies: phantom experiment and confidence interval," *Radio Science*, vol. 46, no. 5, Article ID RS0F08, 2011.
- [16] J. J. Lynch and R. G. Nagele, "Flicker noise effects in noise adding radiometers," *IEEE Transactions on Microwave Theory and Techniques*, vol. 59, no. 1, pp. 196–205, 2011.
- [17] T. Y. Hu, Z. L. Xiao, J. Z. Xu, L. Wu, and T. Y. Hu, "Effects of reverse radiation noise on millimeter-wave radiometric imaging at short range," *Progress in Electromagnetics Research M*, vol. 21, pp. 177–188, 2011.
- [18] S. B. Sharma, D. A. Pujara, S. B. Chakrabarty, and V. K. Singh, "Improving the cross-polar performance of an offset parabolic reflector antenna using a rectangular matched feed," *IEEE Antennas and Wireless Propagation Letters*, vol. 8, pp. 513–516, 2009.
- [19] P.-S. Kildal, "The effects of subreflector diffraction on the aperture efficiency of a conventional Cassegrain antenna—an analytical approach," *IEEE Transactions on Antennas and Propagation*, vol. 31, no. 6, pp. 903–909, 1983.
- [20] M. S. Hersman and G. A. Poe, "Sensitivity of the total power radiometer with periodic absolute calibration," *IEEE Transactions on Microwave Theory and Techniques*, vol. 29, no. 1, pp. 32–40, 1981.
- [21] Y. Han and E. R. Westwater, "Analysis and improvement of tipping calibration for ground-based microwave radiometers," *IEEE Transactions on Geoscience and Remote Sensing*, vol. 38, no. 3, pp. 1260–1276, 2000.
- [22] J.-M. Li, L.-X. Guo, L.-K. Lin, Y.-Y. Zhao, and X.-H. Cheng, "A new method of tipping calibration for ground-based microwave radiometer in cloudy atmosphere," *IEEE Transactions on Geoscience and Remote Sensing*, vol. 52, no. 9, pp. 5506–5513, 2014.



**Hindawi**

Submit your manuscripts at  
<http://www.hindawi.com>

